Title	Molecular dynamics study of instantaneous interfacial thermal resistance of droplets on flat crystalline surface during cooling and ice formation
Author(s)	Ueki, Yoshitaka; Tsutsumi, Yuta; Shibahara, Masahiko
Citation	International Journal of Heat and Mass Transfer. 2022, 194, p. 123004
Version Type	AM
URL	https://hdl.handle.net/11094/88311
rights	© 2022. This manuscript version is made available under the Creative Commons Attribution-NonCommercial-NoDerivatives 4.0 International License.
Note	

Molecular Dynamics Study of Instantaneous Interfacial Thermal Resistance of Droplets on Flat Crystalline Surface during Cooling and Ice Formation

Yoshitaka Ueki[*,§], Yuta Tsutsumi[*] and Masahiko Shibahara[*]

[*]Department of Mechanical Engineering, Osaka University,
2-1 Yamadaoka, Suita, Osaka 565-0871, Japan
[§]Correspondence author. Tel & Fax: +81-6-6879-4987
E-mail: ueki@mech.eng.osaka-u.ac.jp

Abstract

Condensation and frost formation degrade the heat transfer performance of air-conditioners and refrigerators. Yet, the frost formation mechanism has not been fully understood. In the present study, we numerically investigate nanoscale H_2O droplets during cooling and ice formation utilizing classical molecular dynamics simulations. The mW potential is employed for the H_2O molecules. A nanoscale H_2O droplet is placed on a flat solid wall consisting of Pt or Pb atoms. We examine where ice nucleation is formed and how the ice formation proceeds inside the droplet, and then evaluate the time change in instantaneous interfacial thermal resistance between the H_2O molecules and the solid wall. In common with Pt and Pb surfaces, the time changes in the instantaneous interfacial thermal resistance and the density depletion length are qualitatively consistent in the present transient thermal energy transfer process together with the phase change. In addition, the relation of the time-averaged instantaneous interfacial thermal resistance and the density depletion length are qualitatively consistent with the relation of the solid-liquid interfacial thermal resistance in the steady-state.

1. Introduction

Degradation in the performances of air conditioners and refrigerators is caused by frost formation and adhesion on the heat transfer surface. The frost formation process is composed of a dropwise-condensation period, a solidified liquid tip-growth period, and a densification and bulk-growth period [1]. Through those periods, the frost branches form at the top of ice crystals, grow in multiple directions, and then get connected with neighboring frost branches, resulting in the formation of a flat frost layer. A previous experimental observation with X-ray μCT confirmed the above-mentioned frost formation process [2]. Another experimental observation showed that ice formation of a water droplet started from the cooling surface and then a pointy ice tip was formed on the top of the ice drop [3]. Some speculated that the frost branching growth on the top of the ice crystal was because initially volume expansion formed the tip growth during water solidification, and then the ambient humid air induced further condensation, as well as solidification, favorably on the ice tips. Conversely, some reported that the ice formation started from the gas-liquid interface of the water droplet, an ice shell was formed, and then the remaining liquid penetrated from the top of the ice shell as the inner liquid solidified. Despite all the previous experimental studies, the frost formation mechanism has been not comprehensively understood yet.

Some molecular dynamics (MD) studies had been conducted to investigate ice nucleation and growth utilizing classical MD simulations. One of the studies elucidated that the crystal plane orientation of the ice that grew up from the heterogeneous ice nucleation depended on the lattice constant, the plane orientation of the crystalline surface, and the surface wettability [4]. In addition, the ice crystal can have multiple crystal plane orientations such as in the case of ice Ih [5]. Since ice nucleation and growth are complicated phenomena as described above, the thermal energy transport inside the water droplets changes during the cooling and ice formation. On the molecular scale, interfacial thermal resistance (ITR) plays a significant role in thermal energy transport through solid-liquid and solid-solid interfaces. The ITR changes with its interface geometry [6,7], surface wettability [8], and other interface conditions. For example, previous MD studies showed that some surface ornamentations such as nanoparticle layers [9], graphene sheets [10, 11, 12], and self-assembled monolayers [13] on the solid-liquid interface influenced the ITR. Recently, some conducted a spectral analysis based on MD simulations and showed that phonon density of states and spectral heat flux could give further insight into the interfacial thermal transport [14-17]. In most of the previous studies including the above-mentioned ones, the steady-state ITR has been evaluated. For phase change phenomena such as solidification, the transient characterization of the ITR is inevitable. In the case of solidification, the transient characterization of the ITR and the fluid-molecules structuring can be interdependent. Importantly, it is expected that the fluid-molecules structuring determines the droplet solidification process in the frost formation as described above. Also, understanding of the solid-liquid ITR has been limited to the cases without the gas-liquid interfaces, due to its geometric complexity. Especially, characteristics of the instantaneous ITR between the phase-changing droplets and the solid surface have not been comprehensively understood yet. Based on the background, in the present study utilizing the classical MD method, we numerically investigate how a nanoscale water droplet cools down and freezes, and then characterize time changes in instantaneous ITR and interfacial fluid-molecules structuring on flat crystalline planes with different surface characteristics.

2. Numerical Method

Figure 1 illustrates an example of the simulation system employed in the present study. The solid wall consists of Pt or Pb atoms, that have different lattice constants. Pt lattice constant is 392.42 pm. Pb lattice constant is 495.08 pm. In the case of the Pt wall, the simulation cell is 27.74 nm in the *x*-direction, 27.46 nm in the *y*-direction, and 16.96 nm in the *z*-direction. In the case of the Pb walls, the simulation cell is 27.64 nm in the *x*-direction, 27.23 nm in the y-direction, and 17.48 nm in the z-direction. The periodic boundary condition is applied in the *x*- and *y*-directions. The mirror boundary condition is applied on the upper *z*-plane. As an idealized model substrate, the solid wall is a flat crystalline surface. The fluid molecules are H_2O. The ice nucleation rate depends on the plane orientations of the crystalline surface. Especially, the ice nucleations occur favorably on (110) and (111) surfaces of face-centered cubic (fcc) structure [4]. Based on it, we employ the (110) surface of the fcc structure that faces the droplet. The total number of Pt atoms employed in the present simulation is 35000. That of the Pb atoms is 21725. That of the H_2O molecules is 63000. The intermolecular potential for the H_2O molecules is mW potential [18], which is expressed as follows:

$$\phi = \sum_i \sum_{j>i} \varphi_2\left(r_{ij}\right) + \sum_i \sum_{j\neq i} \sum_{k>j} \varphi_3\left(r_{ij}, r_{ik}, \theta_{ijk}\right) \tag{1}$$

$$\varphi_2\left(r_{ij}\right) = A\varepsilon\left[B\left(\frac{\sigma}{r_{ij}}\right)^p - \left(\frac{\sigma}{r_{ij}}\right)^q\right]\exp\left(\frac{\sigma}{r_{ij} - a\sigma}\right) \tag{2}$$

$$\varphi_3\left(r_{ij}, r_{ik}, \theta_{ijk}\right) = \lambda\varepsilon\left[\cos\theta_{ijk} - \cos\theta_0\right]^2 \exp\left(\frac{\gamma\sigma}{r_{ij} - a\sigma}\right)\exp\left(\frac{\gamma\sigma}{r_{ik} - a\sigma}\right) \tag{3}$$

Table 1 mW potential parameters [18].

ε kcal/mol	σ nm	a	λ	γ
6.189	0.23925	1.80	23.15	1.20
$\cos\theta_0$	A	B	p	q
−0.33333	7.04956	0.602225	4.0	0.0

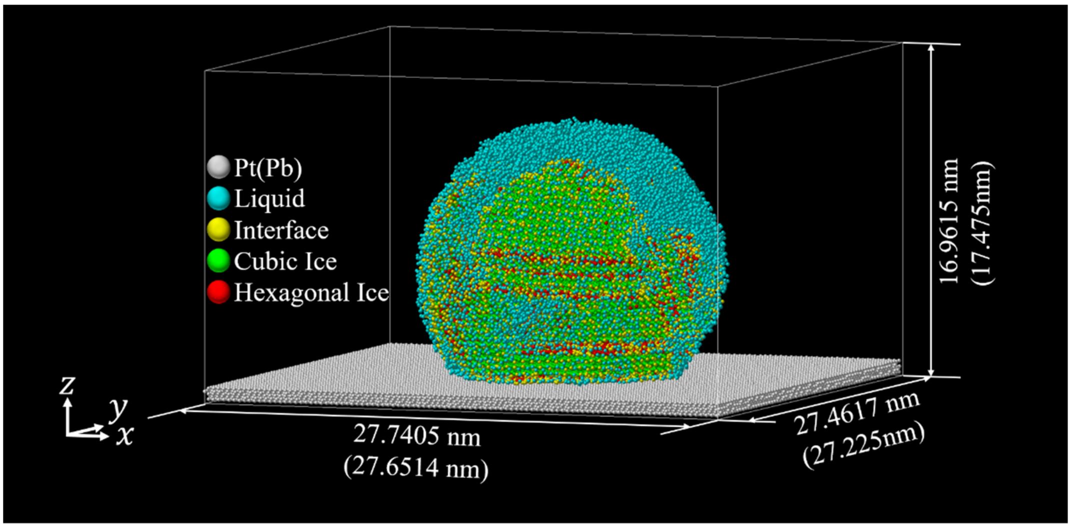

Figure 1. Simulation system.

The mW model is a coarse-grained H_2O model and has been employed to investigate the H_2O phase change phenomena and characteristics [19-21]. It has excellent structural properties and a melting point to experiment [4]. In the present study, we intend to obtain general insight and useful trends regarding the time changes both in the distribution of the H_2O molecules and the instantaneous ITR, during the cooling and ice formation. The mW potential parameters [18] are shown in Table 1. For the pairs of Pt/Pb atoms, we employ the 12-6 Lennard-Jones intermolecular potential as expressed by Eq. (4). Moreover, for the pairs of the Pt/Pb atom and the H_2O molecule, we employ the 12-6 Lennard-Jones potential multiplied with the interaction parameter α, as expressed by Eq. (5). The Lennard-Jones potential has been employed to investigate basic molecular behaviors of solid walls (e.g. [9, 14, 15, 22]) and intermolecular interaction between solid surfaces and fluid molecules (e.g. [9, 14-16, 22]).

$$\phi_{ij}\left(r_{ij}\right)=4\varepsilon\left\{\left(\frac{\sigma}{r_{ij}}\right)^{12}-\left(\frac{\sigma}{r_{ij}}\right)^{6}\right\} \tag{4}$$

$$\phi_{ij}\left(r_{ij}\right)=4\alpha\varepsilon\left\{\left(\frac{\sigma}{r_{ij}}\right)^{12}-\left(\frac{\sigma}{r_{ij}}\right)^{6}\right\} \tag{5}$$

Table 2 Lennard-Jones potential parameters [23].

	σ nm	ε J
Pt - Pt	0.254	1.09×10^{-19}
Pb - Pb	0.3176	2.04×10^{-20}
H_2O - Pt	0.2466	6.85×10^{-20}
H_2O - Pb	0.2784	2.96×10^{-20}

Table 3 Interaction parameter.

Atom	α			
Pt	0.02	0.03	0.04	0.05
Pb	0.04632	0.06948	0.09264	0.1158

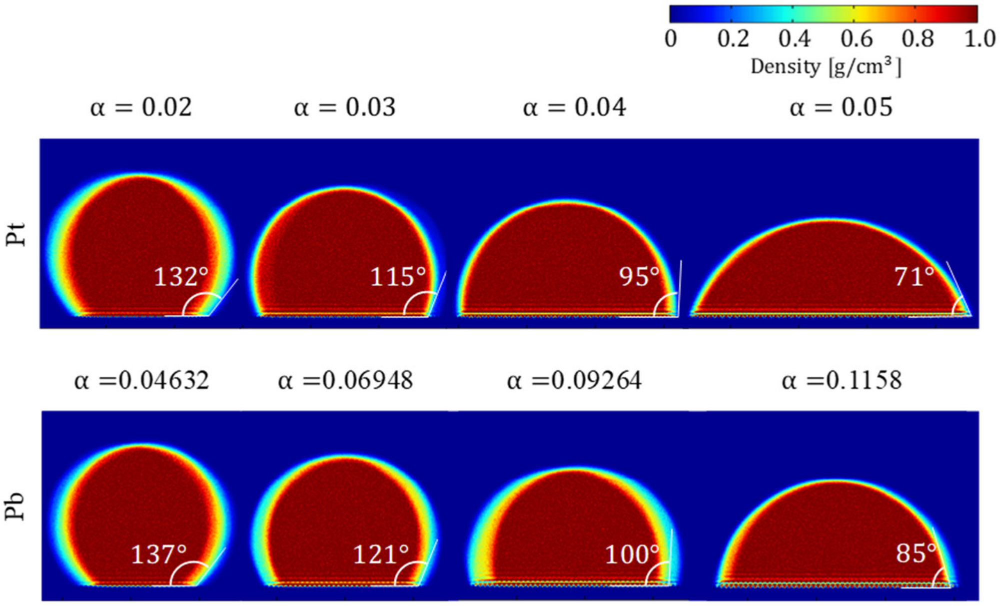

Figure 2. Contact angle at each surface wettability at 280 K.

The Lennard-Jones parameters employed in the present study [23] are shown in Table 2. The products of α and ε are identical in both cases of Pt and Pb. The Lorentz-Berthelot combining rule is employed to determine the potential parameters of the pairs of Pt/Pb and H_2O, σ and ε in the case of $\alpha = 1$ (e.g. [9, 22]). The numerical simulations are performed by LAMMPS [24]. Figure 2 illustrates contact angles of H_2O on the Pt/Pb crystalline surface with different values of α at 280 K. More details of the contact angle evaluation are available in Appendix A. The mass of the Pt atoms is 195.1 g/mol, that of the Pb atoms is 207.2 g/mol, and that of the H_2O molecules is 18.01 g/mol. The time step of the numerical integration is 5.00 fs. The cut-off distance is 10 Å. The numerical integration is performed by the velocity Verlet method. The simulation procedures in the present study are as follows. We employ the Langevin method to control the temperature of the Pt/Pb walls, and the velocity scaling for the H_2O molecules. The solid walls consist of five layers of Pt/Pb atoms. Its outermost layer is fixed. A single layer of phantom atoms is located between the fixed outermost layer and three layers of the solid atoms (see Figure B1). More details are available in Appendix B. In the first relaxation process of 2.5 ns, the H_2O molecules and Pt/Pb atoms are maintained at 280 K by each of the thermostatting methods. Then in the second relaxation process of 2.5 ns, the velocity scaling for the H_2O molecules is removed (see Figure B2). After the relaxation processes, the system reaches the thermal equilibrium judged by velocity distributions of the H_2O molecules. In the cooling and ice formation process, the Pt/Pb atoms are thermostatted at 205 K by the Langevin method. With five different initial configurations of the H_2O molecules, each case was simulated.

We employ the CHILL algorithm to distinguish liquid from crystal [25]. The CHILL algorithm classifies the molecules based on the alignment of their orientation with respect to that of its four closest neighbors into the following group: cubic ice (Ic), hexagonal ice (Ih), interface, and liquid (refer to Appendix C). Its classification coloring is shown in Figure 1. The ITR between the water/ice droplet and the Pt/Pb surface, *R*, is evaluated from the following equation:

$$R = \frac{\Delta T}{q} \tag{6}$$

ΔT denotes the temperature difference between the closest neighbor adsorption layer of the water/ice droplet and the Pt/Pb surface. It is calculated from the time-averaged temperature of the water/ice droplet and the Pt/Pb surface. The time-averaging is 5 ps. The interrogation volume for the temperature calculation is the contact area of the water/ice droplet in the *x*- and *y*-directions, and the 5 Å from the contact plane in the *z*-direction. The interrogation area to determine if the water/ice droplet is in contact with the Pt/Pb surface is 5 Å x 5 Å in the *x*- and *y*-directions (see Figure B3). Its interrogation region in the *z*-direction is z = 0.835 – 1.185 nm in the case of the Pt surface, and z = 1.000 – 1.415 nm in the case of the Pb surface. It is determined by the criteria that the interrogation region includes the nearest adsorption layer of the fluid molecules. The contact area is a sum of the interrogation areas which have one or more fluid molecules in the interrogation region. *q* denotes the temporal heat flux of the thermal energy transferred by the Langevin method over the contact area of the water/ice droplet. At each time step, heat transfer from the Langevin layer is evaluated. Time change rate in the accumulative heat transfer from the Langevin layer is calculated from nine values of the heat transfer from the Langevin layer of four back and forth timestamps, as well as the median timestamp, by using the least square approximation. It is employed to calculate *q* of each median timestamp (see Figure B4).

The solid-liquid ITR, which is the reciprocal of thermal boundary conductance, is proportional to the density depletion length (DDL) in the combination of some solid-liquid interfaces (e.g. [26-29]). The DDL has been the qualification of equilibrium distance between phases. It is evaluated from the following relation:

$$\delta = \int_0^{\infty} \left(1 - \frac{\rho_s(z)}{\rho_s^b} - \frac{\rho_L(z)}{\rho_L^b}\right) dz \tag{7}$$

In the present study, we divide the droplet volume at regular intervals in the z-direction and evaluate instantaneous droplet density profiles by distinguishing the gas-liquid interface of the droplets. From them, we obtain instantaneous DDL of the H_2O droplets. In both cases of Pt and Pb surfaces, the droplets are being cooled down by contacting solid surfaces and reach supercooling states before the ice nucleation and growth. The droplet temperatures are shown in Appendix D. The melting point of mW water is 274.6 K [18].

3. Results

3.1 Ice Nucleation and Growth

Figure 3 illustrates typical examples of the snapshots of the temporal cross-section of the H_2O droplet on the Pt surface during the ice formation in the case that α = 0.02 and 0.05. The white circles represent the ice nucleation site where the ice keeps growing up. In the present Pt-H_2O system, heterogeneous ice nucleation occurs on the Pt surface. In the case of a better wettability surface, more ice nucleation occurs at a faster rate. One of its reasons is that the droplet spreads on the Pt surface and the contact area increases. In Figure 3, the white arrows inside the droplets represent the ice formation direction. The ice formation proceeds from the Pt surface toward the droplet tip. The ice structure formed in the present study is a laminate structure of the hexagonal and cubic ices. In the case of the relatively poor wettability of α = 0.02, the laminate structure grows up in the off-vertical direction with respect to the Pt surface. It is because less ice nucleation happens on the poor wettability surface. In the case of the relatively better wettability surface, simultaneously multiple ice nucleations happen. In the ice growing period, they merge and then grow up in the vertical direction. In the Pb-H_2O system, similarly to the Pt-H_2O one, the heterogeneous ice nucleation happens on the Pb surface except in the most hydrophobic case of α = 0.04632. In this case, homogeneous ice nucleation happens as well as heterogeneous one. Figure 4 illustrates the time change in the fraction of the ice, which is the sum of fractions of the cubic, hexagonal, and interface, at different values of α, in the Pt- and Pb-H_2O systems. For each case, we perform the above-mentioned simulations under five different initial conditions. Those averaged values and error bars are shown. The standard variances are shown as the error bars in light colors. It shows that, as the surface has better wettability, the ice nucleation occurs earlier and the ice formation proceeds faster. In addition, note that the saturated ice fraction is approximately 0.9 and the remaining part is in a form of a liquid or amorphous state. We find that the earlier ice nucleation happens on the Pt surface than on the Pb one. It depends on the lattice constant (e.g. [5]). Figure 5 shows typical examples of the snapshots of the cross-section of the ice droplets in the steady-state. From Figure 5, there are some liquid/amorphous molecules inside the ice droplets. The quasi-liquid state, where the water molecules stay melted even under the solidification temperature, can be seen on the ice interface [30]. Furthermore, amorphous ice can form from supercooled water [31]. The quasi-liquid layer or/and the amorphous ice is formed inside the ice droplet, and so the ice droplet is not completely in the crystalline forms. The topological defect structure of the ice with the 5-fold symmetry is found when the homogeneous ice nucleation occurs in the case of the Pb surface at α = 0.04632 (See Figure 5 (c)). A similar topological defect structure is reported in the previous study [32]. Figure 6 illustrates typical examples of the plane orientations of the ice formed on the Pt/Pb surfaces. It shows that, with different lattice constants, the formed ice has different plane orientations. In the Pt-H_2O system, the ice plane orientations are $\{10\bar{1}0\}$ in the *x*-*z* plane, and $\{11\bar{2}0\}$ in the *y*-*z* plane. We find that a laminated ice structure of the hexagonal and the cubic ice on the Pt surface where the heterogeneous ice nucleation occurs and the ice growth plane proceeds perpendicularly. Similarly, a laminated structure is found in the Pb-H_2O system as well. As a difference, the plane orientations are $\{11\bar{2}0\}$ in the *x*-*z* plane, and $\{0001\}$ in the *y*-*z* plane.

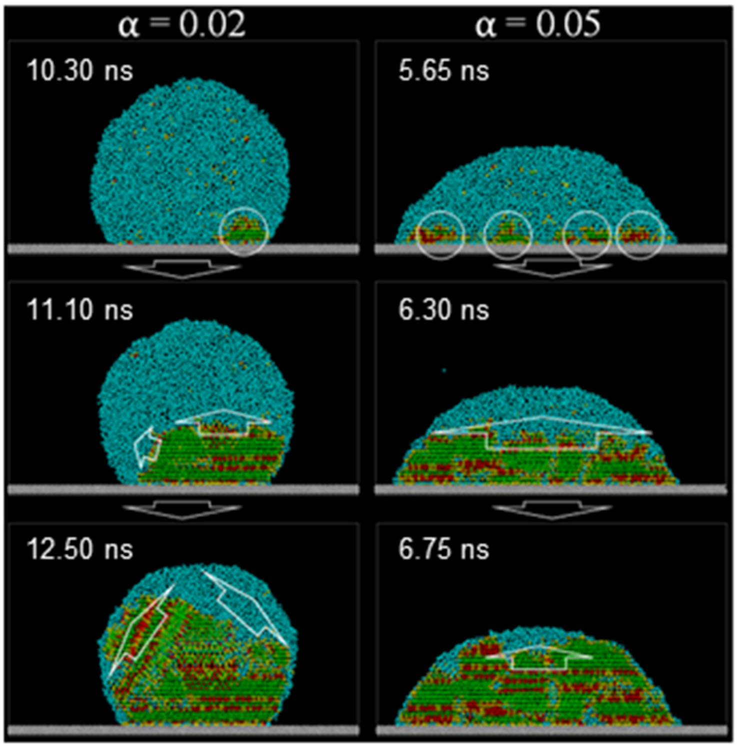

Figure 3. Snapshots of temporal cross-section of water droplet on Pt surface during ice formation; molecule coloring is based on classification of CHILL algorithm in the cases of α = 0.02 and 0.05; The timestamps of each snapshot are shown in the upper left corner. The

white circles represent the ice nucleation points. The white arrows inside the droplets represent the ice formation direction.

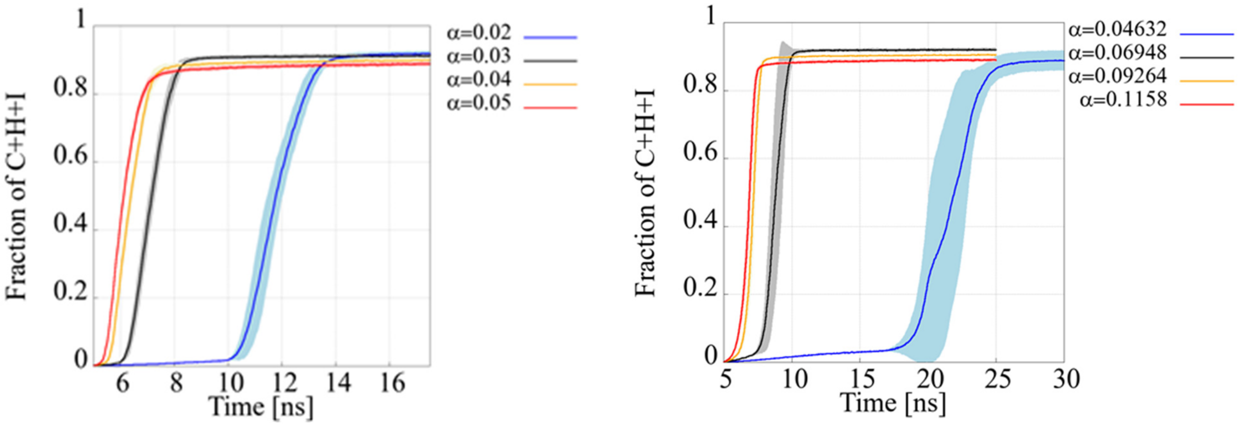

(a) Pt-H_2O system (b) Pb-H_2O system

Figure 4. Time change in the fraction of ice, which is the total fraction of cubic, hexagonal, and interface, at different values of α.

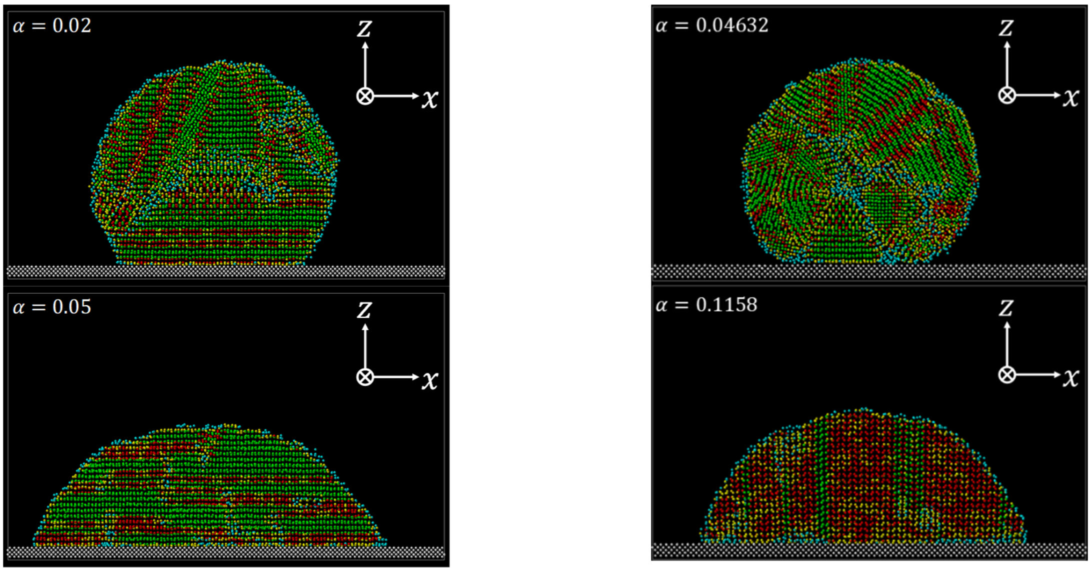

(a) Pt-H_2O system (b) Pb-H_2O system

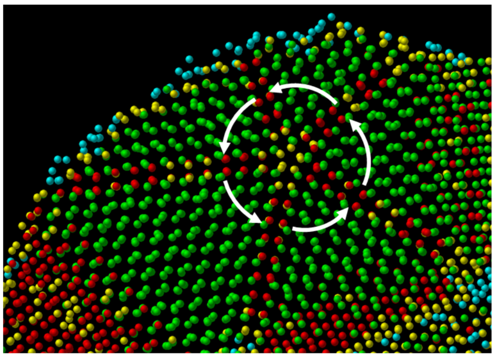

(c) Topological defect structure of ice with 5-fold symmetry;
Pb-H_2O system in the case of α = 0.04632.

Figure 5. Snapshots of cross-section of ice droplets in steady-state; molecule coloring is based on classification of CHILL algorithm.

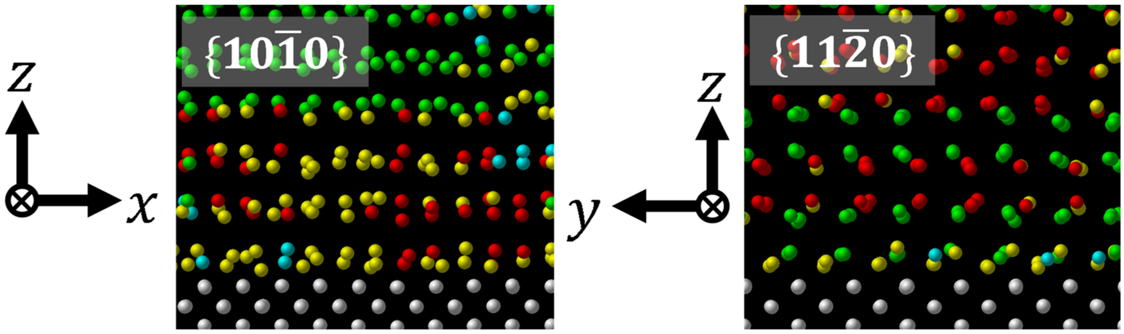

(a) Pt-H_2O system

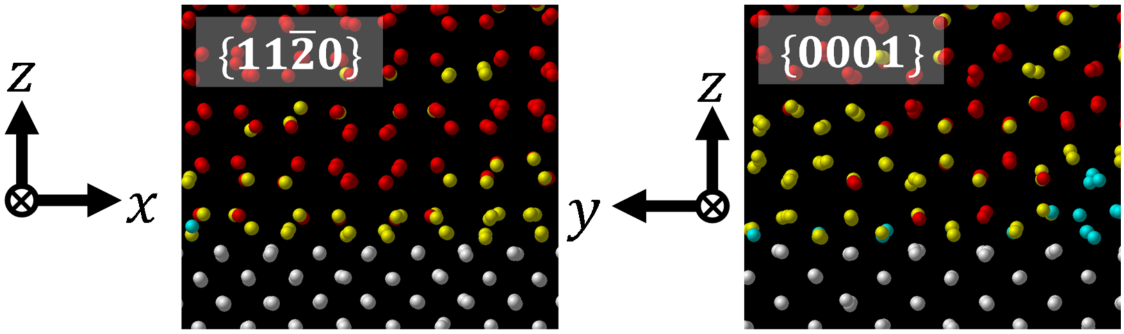

(b) Pb-H_2O system

Figure 6. Plane orientations of ice formed on Pt/Pt surfaces; molecule coloring is based on classification of CHILL algorithm.

3.2 Relation of instantaneous ITR, DDL, and Ice Fraction

Figure 7 illustrates the time change in the instantaneous ITR, DDL, and the ice fraction in the Pt-H_2O system. For each value of α, we perform the above-mentioned simulations under five different initial conditions. Those averaged values and error bars are shown in Figure 7. The standard variances are shown as the error bars in light colors. Similarly, Figure 8 illustrates the time change in the ITR, DDL, and the ice fraction in the Pb-H_2O system. In the case of $\alpha = 0.04632$, homogeneous ice nucleation and growth occur. The way of the droplet freezing in the cases of homogeneous ice nucleation differs from that in the cases of the heterogeneous ice nucleation. Therefore, the ITR-DDL relation cannot fairly be compared between them. In the present study, we focus on the cases of heterogeneous ice nucleation. To align the comparison conditions, the case of $\alpha = 0.04632$ is not considered for the investigation of the ITR-DDL relation. In the case of $\alpha = 0.06948$, homogeneous nucleation and growth occur one out of five times. For the purpose of the present study described above, the case is omitted from the data averaging and drawing.

In the present study, the difference in α induces the different trends of the ITR. From Figures 7 and 8, we find the trend that the time change in the instantaneous ITR mostly follows that in the instantaneous DDL. Based on this, we conclude that the time changes in the instantaneous ITR and DDL are qualitatively consistent in the present transient thermal energy transfer process. Moreover, in the cooling and following supercooling processes, the DDL decreases. After the ice nucleation and growth from the solid walls, the DDL increases. The ice crystals of the mW potential have less density than those in the liquid state. Also, the DDL greatly fluctuates. Due to the ice crystal formation, the instantaneous H_2O molecule density profiles show dense and coarse parts, which fluctuate as well. We speculate that it causes a great DDL fluctuation in the ice formation process.

In the present study, the order of magnitude of the ITR is from 10^{-9} to 10^{-8} m^2K/W. It is consistent with the previous study of the ITR between the mW H_2O molecules and the Lennard-Jones Pt surface [33, 34]. In the study, the order of magnitude of the ITR was 10^{-8} m^2K/W. Note that the plane orientation of the Pt crystalline surface and some of the other conditions are not identical. According to the other previous studies, the order of magnitude of the solid-liquid ITR was from 10^{-9} to 10^{-7} m^2K/W, depending on the definitions of the thermal resistance, the surface wettability, and the fluid molecular models [e.g., 6-16, 35-37]. The order of magnitude of the ITR in the present study is consistent with the above-mentioned previous studies. The following relation of the ITR and DDL is given, where the fitting parameters A_{TBC} = 195 MW/m^2K, and n =11.59 nm^{-1} [26]:

$$R = 1/G = 1/A_{\mathrm{TBC}}\, e^{-n\delta} \tag{8}$$

Note that the fitting parameters can differ depending on the combination of the neighboring solid and liquid, such as SiC-H_2O [27], Al_2O_3-H_2O [29], and graphite-H_2O [38] systems. In the case of Ref [26], the interface was the Si-H_2O system, where Tersoff potential was employed for the Si, and the SPC/E potential was for H_2O. Different plane orientations of the silicons walls were included in fitting Eq. (8). Among the previous studies, it is the closest combination with respect to the present study, and we conclude that it is possible to qualitatively verify the present study by comparing it. For further comparison, we evaluate the solid-liquid ITR and DDL of the liquid film system in the steady-state (for more details, see Appendix E).

Figure 9 illustrates the time-averaged ITR and DDL of the freezing droplet system with respect to Eq. (8). The instantaneous ITR and DDL are averaged from the main calculation start (5 ns) to the point where the ice fraction reaches 0.5. The standard deviations are shown as error bars in Figure 9. In a large part, the present results of the droplets in the cooling and ice formation processes are consistent with the solid-liquid ITR-DDL relation in the steady state. We speculate that the slight differences between the present results and the relation of Eq. (8) arise from that the H_2O molecules are supercooled and then solidifying. The ice formation causes less dense molecular structures, which increases DDL. Also, note that originally the ITR-DDL relation was given just for the solid-liquid system in the steady-state thermal conduction. In the case of $\alpha = 0.05$ in the Pt-H_2O system, the time-averaged ITR decreases compared with that of $\alpha = 0.04$, even though the time-averaged DDL increases. In this case, due to the relatively high wettability and intermolecular interaction, the ice nucleation and growth start immediately just after the droplet cooling begins. In the Pt-H_2O system, the DDL of the ice state tends to be greater than that of the liquid state. It influences the time-averaged ITR and DDL relation in the case of $\alpha = 0.05$. On the other hand, in the Pb-H_2O system, the DDL of the ice state tends to be less than that of the liquid state. We speculate that the difference in the DDL trends arises from the plane orientations of the ice formed on each kind of surface, as shown in Figure 6. In the case of $\alpha = 0.1158$ in the Pb-H_2O system, the time-averaged ITR and the DDL are lower than the others. We speculate that the difference in the ice plane orientations on the solid walls influences the ITR-DDL relation as well.

For the comparison, the steady-state solid-liquid ITR of the liquid film system is shown in Figure 9. The steady-state ITR of the Pt-H_2O (liquid film) system is consistent with the previous study [33, 34], and we speculate that the slight difference is mainly caused by the plane orientation of the Pt walls. We find that the relation of ITR and DDL in the steady-state can be expressed by Eq. (8) with different fitting parameters. From Figure 9, in the liquid film system, the ITR in the case of the Pt wall is higher than that of the Pb one at the same value of the DDL. We speculate that the trend is caused by the difference in the lattice constant because a wider lattice constant allows less density depletion space between the solid wall and the existence domain of the fluid molecules. In addition, we can see that the DDL of the liquid film system is lower than that of the droplet system. In the liquid film system, the fluid molecules are confined by the walls, which decreases the DDL. However, in the droplet system, free space surrounds the droplet, which may allow the longer DDL.

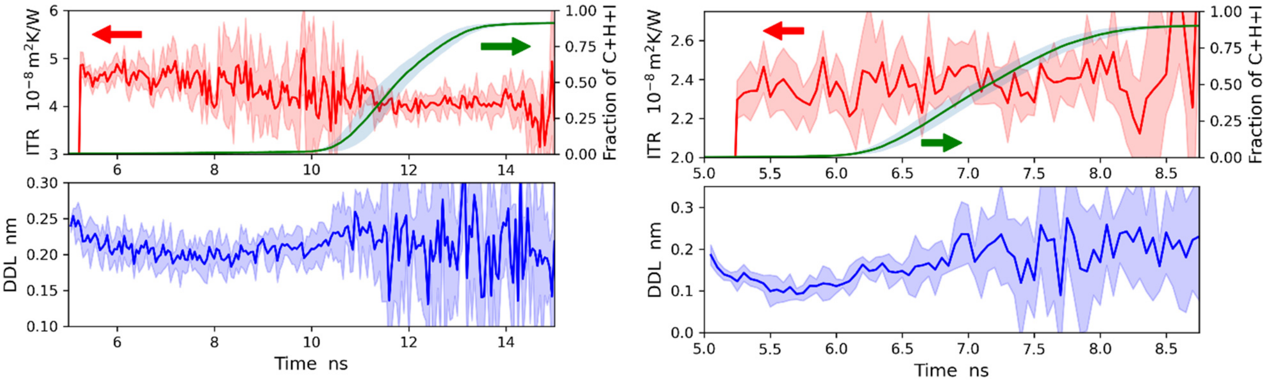

(a) $\alpha = 0.02$

(b) $\alpha = 0.03$

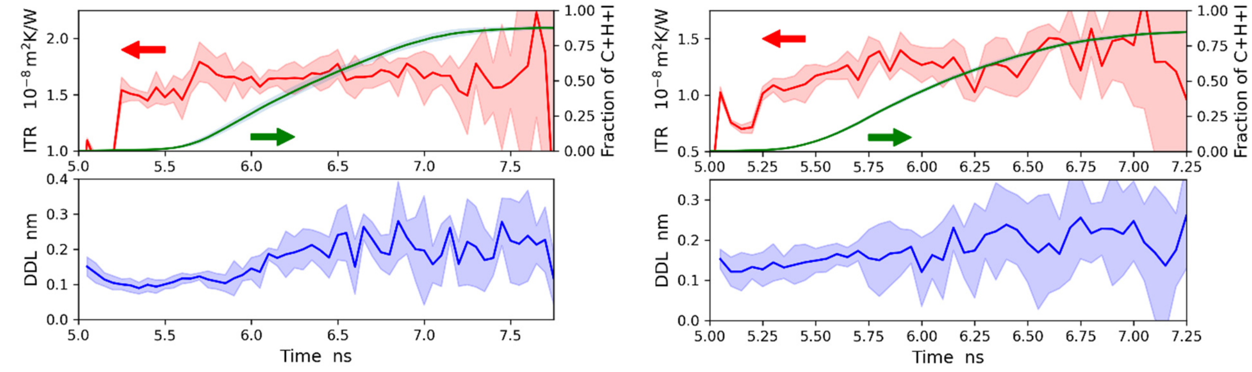

(c) $\alpha = 0.04$

(d) $\alpha = 0.05$

Figure 7. Instantaneous ITR, DDL, and ice faction during cooling and ice formation in the Pt-H_2O system.

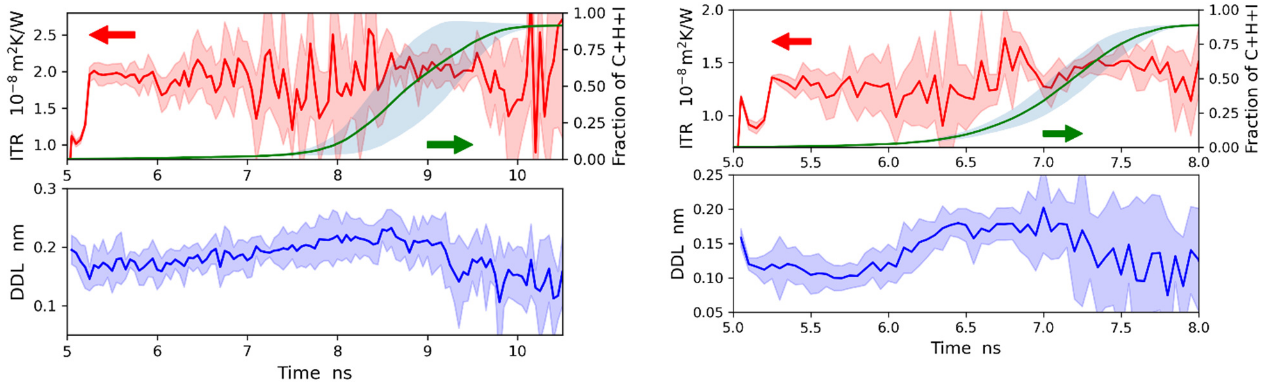

(a) $\alpha = 0.06948$

(b) $\alpha = 0.09264$

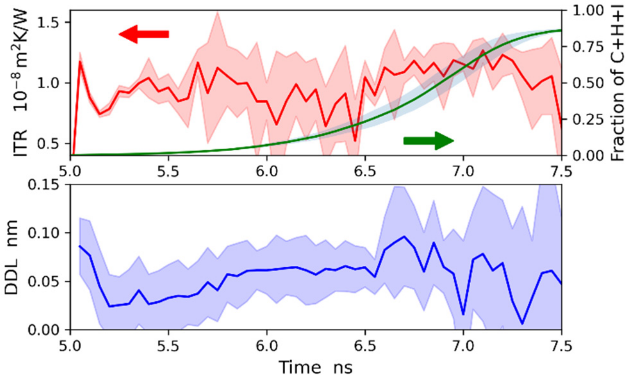

(c) $\alpha = 0.1158$

Figure 8. Instantaneous ITR, DDL, and ice faction during cooling and ice formation in the Pb-H_2O system.

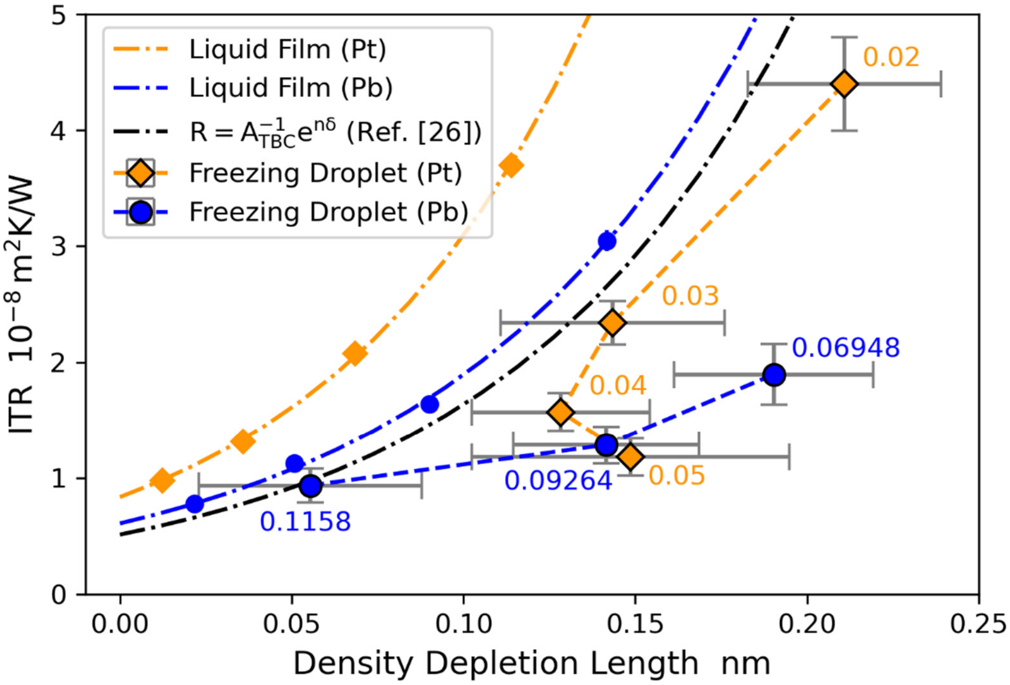

Figure 9. Relation of time-averaged ITR and DDL.

4. Conclusions

Utilizing classical MD simulations, we numerically investigate how the nanoscale water droplet cools down and freezes. We characterize the transient behaviors of the instantaneous ITR and the fluid-molecules structuring of the phase-changing droplet on the crystalline planes with the different surface characteristics. Our findings are summarized as follows.

In the Pt-H_2O system, the heterogeneous ice nucleation occurs favorably on the Pt surface, and the ice formation proceeds toward the droplet tip. On the relatively better wettability surface, the multiple ice nucleation occurs early and simultaneously. On the relatively poor wettability surface, biased ice formation happens. In the Pb-H_2O system, relatively-late ice nucleation and growth are found. In the least wettability examined in the present study, the homogeneous ice nucleation and growth happen. The characteristics of the ice nucleation and growth depend on the lattice constant as well as the surface wettability.

In common with Pt and Pb surfaces, the time changes in the instantaneous ITR and DDL are qualitatively consistent in the present transient thermal energy transfer process together with the phase change. In the cooling and following supercooling processes, the DDL decreases. After the ice nucleation and growth from the solid walls, the DDL increases. The Other transient characteristics depend on the surface wettability and the lattice constant.

The ITR and DDL, which are time-averaged from the start of the cooling to the point where the ice fraction of the droplet reaches half, are qualitatively consistent with the previously-reported relation of the solid-liquid ITR in the steady-state. With better surface wettability, earlier ice nucleation and growth happen. Especially in the most hydrophilic case of the Pt surface, it causes the exceptional trend that the lower time-averaged ITR, even though the time-averaged DDL increases.

Appendix

A. Contact Angle Evaluation

Figure A1 illustrates the simulation model to evaluate the contact angle of the columnar H_2O droplet. The total number of Pt atoms employed is 6000, and that of the Pb atoms is 3950. That of the H_2O molecules is 16800. The simulation cell size is 27.7405 nm ×4.70772 nm ×16.9615 nm in the case of the Pt surface. In the case of the Pb surface, it is 27.6514 nm ×4.95 nm ×17.475 nm. The periodic boundary condition is applied in the *x*- and *y*-directions. The mirror boundary condition is applied on the upper *z*-plane. The Pt/Pb atoms are maintained at 280K by the Langevin method. In the first relaxation process of 0.5 ns, the velocity scaling is applied to the H_2O molecules, together with the Langevin thermostat of the solid wall. The target temperature is 280 K. Without the velocity scaling of the H_2O molecules, the second relaxation process of 7 ns is performed. After this, the density distribution of the H_2O droplet is evaluated by taking a time average of 2.5 ns. The time step of the numerical integration is 5.00 fs. The numerical integration is performed by the velocity Verlet method. The contact angle evaluation is based on the $\theta/2$ method.

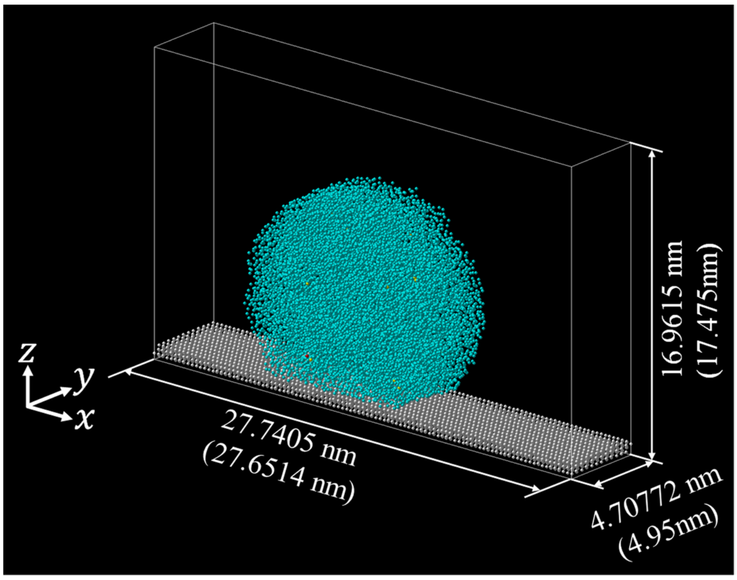

Figure A1. Simulation model.

B. Numerical Method

Figure B1 illustrates the Langevin thermostat. The phantom particles are given the intermolecular force, the damping force expressed by Eq. (B1), and the random force expressed by Eq. (B2).

$$F_\mathrm{f} = -\frac{m_i}{\gamma} v_i \tag{B1}$$

$$F_r \propto \sqrt{\frac{k_B T m_i}{\gamma \Delta t}} \tag{B2}$$

m_i denotes the mass of the phantom particle, γ does the damping factor of 200.0, v_i does the translational velocity of the particle, T does the target temperature, and Δt does the time step.

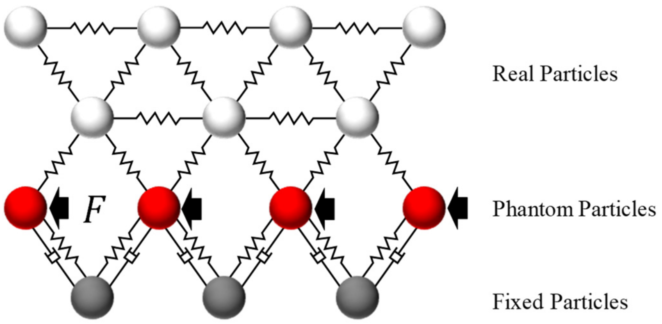

Figure B1. Langevin thermostat.

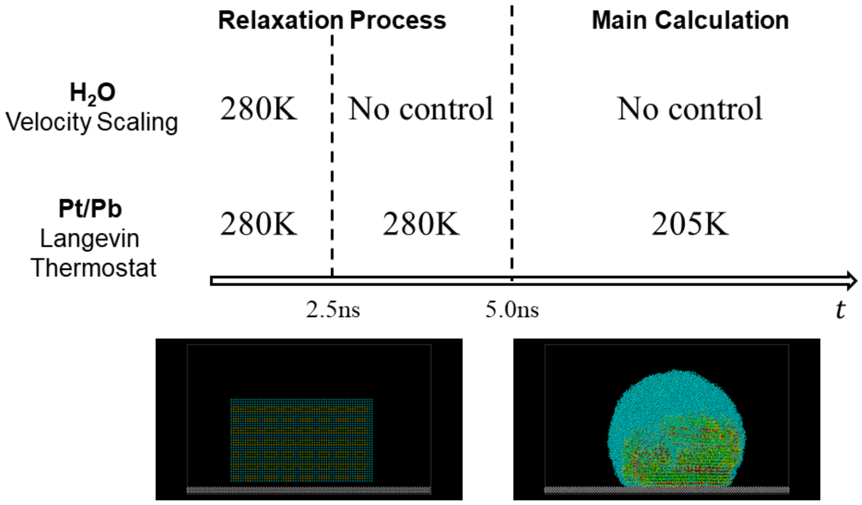

Figure B2. Numerical procedures.

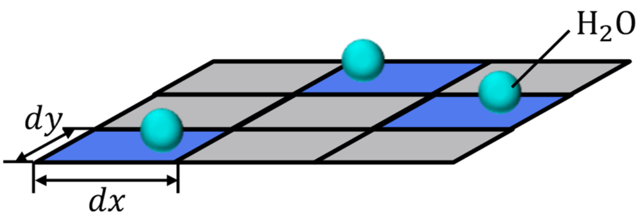

Figure B3. Schematic diagram of calculation method of the contact area.

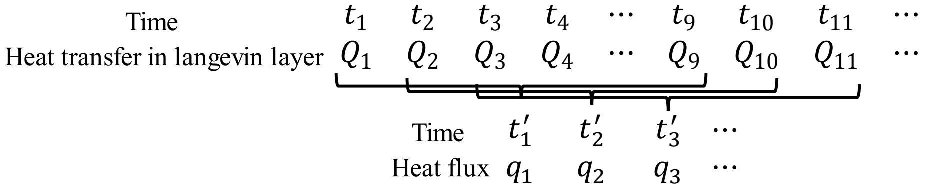

Ex) t'_1 = Median from t_1 to t_9

$$q_1 = \frac{9\sum_{i=1}^{9} t_i Q_i - \sum_{i=1}^{9} t_i \sum_{i=1}^{9} Q_i}{9\sum_{i=1}^{9} t_i^2 - \left(\sum_{i=1}^{9} t_i\right)^2} \frac{1}{A(t'_1)} \text{ (Least-squares method)}$$

Figure B4. Calculation method of heat flux at solid-liquid interface.

C. CHILL Algorithm

The CHILL algorithm is based on Ref [25]. For each H_2O molecule, unit vectors with respect to its neighboring molecules, $\hat{r}_{ij}$, are evaluated. The subscript of *i* denotes the classification target molecule, and the subscript of *j* denotes the closest neighboring molecules. With the spherical harmonics function, $Y_{l,m}$, the following parameters are calculated:

$$q_{lm}(i) = \frac{1}{4}\sum_{j=1}^{4} Y_{l,m}(\hat{r}_{ij}) \tag{C1}$$

$$a(i,j) = \frac{\sum_{m=-l}^{l} q_{lm}(i) q_{lm}^*(j)}{\left(\sum_{m=-l}^{l} q_{lm}(i) q_{lm}^*(i)\right)^{1/2} \left(\sum_{m=-l}^{l} q_{lm}(j) q_{lm}^*(j)\right)^{1/2}} \tag{C2}$$

If $a(i,j) < -0.80$, the two-body bond is categorized as the staggered bond. If $-0.20 < a(i,j) < -0.05$, the bond is categorized as the eclipsed bond. The group classification is based on conditions shown in Table C1.

Table C1. Classification conditions in CHILL algorithm.

Group	**Conditions**
Cubic ice (I_c)	staggered bonds for all *j*
Hexagonal ice (I_h)	staggered bonds for three *j* and eclipsed bond for one *j*
Interface	(i) or (ii) (i) staggered bonds for only two *j* and at least one neighbor with more than two staggered bonds (ii) staggered bonds for three *j* and no eclipsed bond for any *j* and at least one neighbor with two staggered bonds
Liquid	Others

D. Time Change in Droplet Temperature

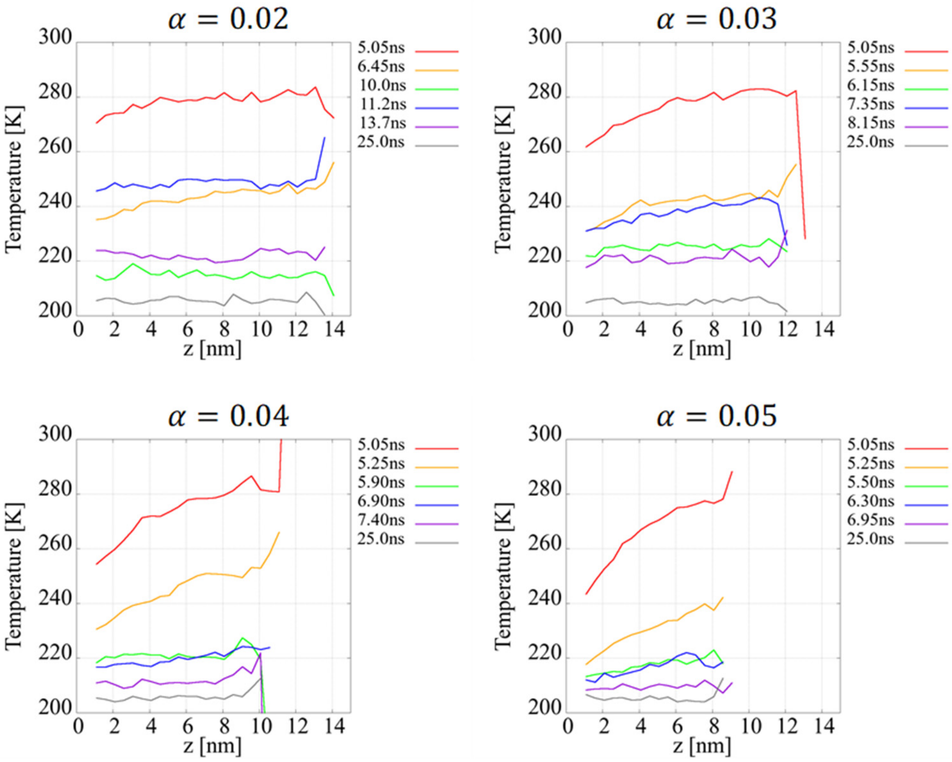

Figure D1. Time change in droplet temperature distribution in z-direction in Pt-H_2O system.

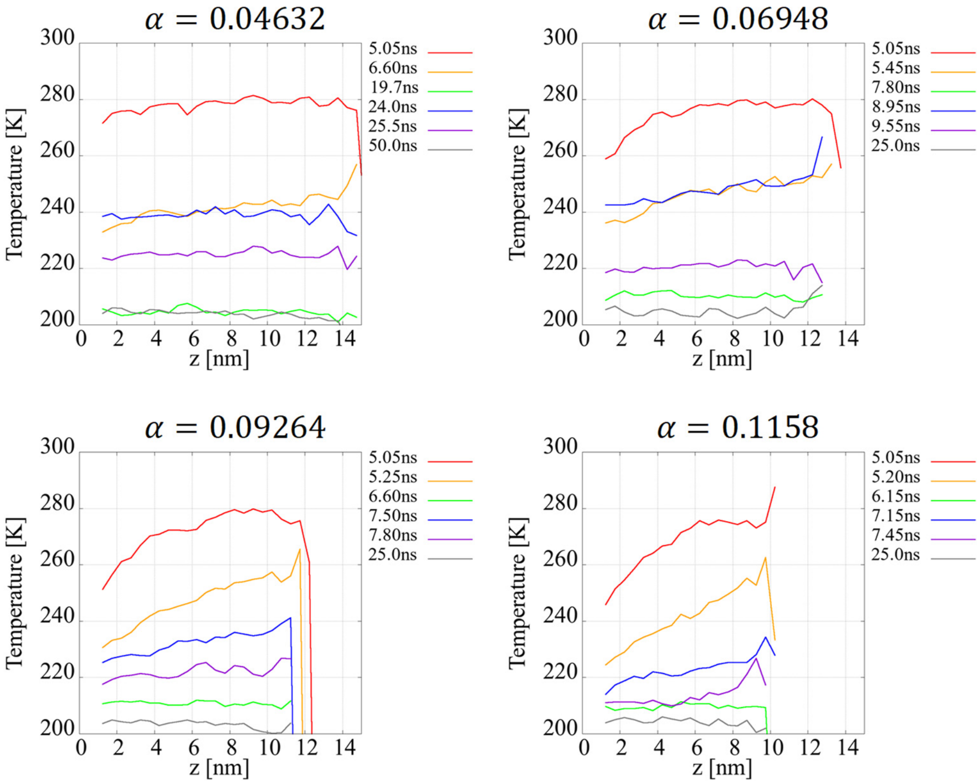

Figure D2. Time change in droplet temperature distribution in z-direction in Pb-H_2O system.

E. Solid-Liquid ITR in Steady-State

We evaluated the solid-liquid ITR in the steady-state. Figure E1 illustrates an example of the simulation system. A liquid film of H_2O molecules is confined by parallel walls. The solid wall consists of Pt or Pb atoms. The upper and lower walls have the Langevin thermostats. The lower thermostat temperature is 300K, and the upper one is 350K. The parameter settings for the solid walls are identical to those of the above-mentioned droplet system. In the case of the Pt wall, the simulation cell is 8.32 nm in the *x*-direction, and 7.84 nm in the *y*-direction. The height of the simulation cell varies from 7.88 to 8.05 nm so that the system pressure stays in the target range of 0 – 5 MPa. The total number of Pt atoms is 6000, and that of H_2O molecules is 13457. In the case of the Pb walls, the simulation cell is 8.05 nm in the *x*-direction, and 7.92 nm in the y-direction. The height of the simulation cell varies from 9.60 to 9.82 nm. The periodic boundary condition is applied in the *x*- and *y*-directions. The total number of Pb atoms is 3680, and that of H_2O molecules is 16000. The numerical method and settings including the intermolecular potentials are identical to those of the above-mentioned droplet system as well. The interaction parameter of α changes to four values similarly to the droplet system. The numerical procedure is that, in the first period of 0 – 0.05 ns, the velocity scaling of 325K is applied to H_2O molecules and the Langevin thermostats works, in the second period of 0.05 – 2.05 ns, the relaxation process is performed only with the Langevin thermostats, and then in the third period of 2.05 – 7.05 ns, the main calculation is performed continuously with the Langevin thermostats. In the main calculation, the steady-state temperature gradient and density distributions are obtained and employed to evaluate the ITR and DDL. We perform the above-mentioned simulations under three different initial conditions. Those averaged values and error bars are shown in Figure 9.

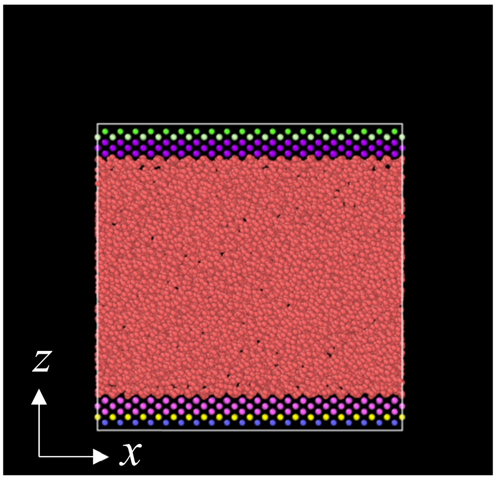

Figure E1. Simulation system: Liquid film system.

Nomenclature

a	mW potential parameter for two-body and three-body interactions
A	mW potential paramter for two-body interaction
A_{TBC}	fitting parameter in thermal boundary conductance
B	mW potential paramter for two-body interaction
G	thermal boundary conductance
i, j, k	molecular index
n	fitting parameter in thermal boundary conductance
p	mW potential parameter for two-body interaction
q	heat flux or mW potential parameter for two-body interaction
r	intermolecular distance
R	interfacial thermal resistance
x, y, z	Cartesian coordinates
α	interaction parameter
δ	density depletion length
γ	mW potential paramter for three-body interaction
ΔT	temperature difference
ε	depth of intermolecular potential well in LJ potential or mW potential parameter for two-body and three-body interactions
θ_{ijk}	bonding angle of molecular *i*, *j*, *k* in mW potential
θ_0	mW potential parameter for three-body interaction
λ	mW potential parameter for three-body interaction
σ	apparent molecular radius in LJ potential or mW potential parameter for two-body and three-body interactions
ρ	density
ϕ	intermolecular potential

Subscript

S	solid
L	liquid

Superscript

b	bulk

Declaration of Competing Interest

We have no conflicts of interest to disclose.

CrediT Authorship Contribution Statement

Yoshitaka Ueki: Investigation, Methodology, Software, Formal analysis, Visualization, Data curation, Validation, Writing – Original Draft, Reviewing & Editing
Yuta Tsutsumi: Investigation, Methodology, Software, Formal analysis, Visualization, Data curation, Validation, Writing - Review & Editing
Masahiko Shibahara: Conceptualization, Methodology, Resources, Writing – Reviewing & Editing, Supervision, Project administration, Funding acquisition

Acknowledgment

This work was supported by JSPS KAKENHI Grant Number 18H01382. The authors wish to thank Ryota Kashiwagi of Osaka University for technical help in analyzing the ITR-DDL relation in the case of the liquid-solid interface by using the MD simulation.

References

[1] M. Song, C. Dang, “Review on the measurement and calculation of frost characteristics”, International Journal of Heat and Mass Transfer, **124**, pp. 586-614 (2018).

[2] R. Matsumoto, T. Uechi, Y. Nagasawa, “Three-dimensional microstructure of frost layer measured by using X-ray μCT”, Journal of Thermal Science and Technology, **13(1)**, (2018).

[3] A. G. Marín, O. R. Enríquez, P. Brunet, P. Colinet, J. H. Snoeijer, “Universality of tip singularity formation in freezing water drops”, Physical Review Letters, **113,** 054301 (2014).

[4] M. Fitzner, G. C. Sosso, S. J. Cox, A. Michaelides, “The many faces of heterogeneous ice nucleation: interplay between surface morphology and hydrophobicity”, Journal of American Chemical Society, **137**, 42, 13658–13669 (2015).

[5] J. A. Hayward, A. D. J. Haymet, “The ice/water interface: Molecular dynamics simulations of the basal, prism, $\left\{20\bar{2}1\right\}$, and $\left\{2\bar{1}\bar{1}0\right\}$ interfaces of ice Ih”, Journal of Chemical Physics, **114**(8), 3717-3726 (2001).

[6] Y. Wang, P. Kebliski, "Role of wetting and nanoscale roughness on thermal conductance at liquid-solid interface", Applied Physics Letters, **99** 073112 (2011).

[7] M. Shibahara et al., "Molecular Dynamics Study on Influences of Surface Structural Characteristics on Thermal Energy Transport over Liquid-Solid Interfaces", International Heat Transfer Conference Digital Library (2014). DOI: 10.1615/IHTC15.mlt.008513

[8] Z. Ge et al., "Thermal Conductance of Hydrophilic and Hydrophobic Interfaces", Physical Review Letters, 96, 186101 (2006).

[9] Y. Ueki, Y Miyazaki, M Shibahara, T Ohara "Molecular dynamics study of thermal resistance of solid-liquid interface in contact with single layer of nanoparticles", International Journal of Heat and Mass Transfer, **120,** 608-623 (2018).

[10] A. T. Pham et al., "Interfacial thermal resistance between the graphene-coated copper and liquid water", International Journal of Heat and Mass Transfer, **97**, 422-431 (2016).

[11] D. Alexeev, J. Chen, J. H. Walther, K. P. Giapis, P. Angelikopoulos, P. Koumoutsakos, “Kapitza Resistance between Few-Layer Graphene and Water: Liquid Layering Effects”, Nano Letters, **15**, 5744-5749 (2015).

[12] X. Peng, P. Jiang, Y. Ouyang, S. Lu, W. Ren, J. Chen, “Reducing Kapitza resistance between graphene/water interface via interfacial superlattice structure”, Nanotechnology, **33**, 035707 (2022).

[13] G. Kikugawa et al., "A molecular dynamics study on heat transfer characteristics at the interfaces of alkanethiolate self-assembled monolayer and organic solvent", Journal of Chemical Physics, **130**, 074706 (2009).

[14] A. Giri, P. E. Hopkins, "Spectral analysis of thermal boundary conductance across solid/classical liquid interfaces: A molecular dynamics study", Applied Physics Letters, **105,** 033106 (2014).

[15] K. Sääskilahti et al., "Spectral mapping of heat transfer mechanisms at liquid-solid interfaces", Physical Review E, **93**, 052141 (2016).

[16] B. Ramos-Alvarado, S. Kumar, "Spectral Analysis of the Heat Flow Across Crystalline and Amorphous Si–Water Interfaces", The Journal of Physical Chemistry C, **121**(21) 11380-11389 (2017).

[17] W. Ren, Y. Ouyang, P. Jiang, C. Yu, J. He, J. Chen, “The Impact of Interlayer Rotation on Thermal Transport Across Graphene/Hexagonal Boron Nitride van der Waals Heterostructure”, Nano Letters, **21** (6), 2634-2641(2021).

[18] V. Molinero et al., "Water Modeled As an Intermediate Element between Carbon and Silicon", Journal of Physical Chemistry B, **113**(13) (2009) 4008-4016.

[19] M. Fitzner et al., "Predicting heterogeneous ice nucleation with a data-driven approach", Nature Communications, **11**:4777 (2020).

[20] R. Shi and H. Tanaka, "The anomalies and criticality of liquid water", PNAS, **117** (43) 26591-26599 (2020).

[21] L. Lupi et al., "Role of stacking disorder in ice nucleation", Nature, **551**, 218–222 (2017).

[22] Y. Ueki et al., “Molecular dynamic study of evaporation in nanoslit: Influence of slit geometry and wettability”, International Journal of Heat and Mass Transfer, 120463 (2021).

[23] S. B. Zhu et al., "Interaction of water with metal surfaces", The Journal of Chemical Physics, **100**(9), 6961-6968 (1994).

[24] S. Plimpton, “Fast Parallel Algorithms for Short-Range Molecular Dynamics”, Journal of Computational Physics, **117**, 1-19 (1995).

[25] E. B. Moore et al., “Freezing, melting and structure of ice in a hydrophilic nanopore”, Physical Chemistry Chemical Physics, **12**, 4124-4134 (2010).

[26] B. Ramos-Alvarado et al., “Solid-Liquid Thermal Transport and Its Relationship with Wettability and the Interfacial Liquid Structure”, J. Phys. Chem. Lett., **7** (17), 3497–3501 (2016).

[27] C. U. Gonzalez-Valle, S. Kumar and B. Ramos-Alvarado, “Thermal Transport across SiC–Water Interfaces”, ACS Appl. Mater. Interfaces, **10**(34), 29179–29186 (2018).

[28] S. Li et al., “Atomic structure causing an obvious difference in thermal conductance at the Pd–H2O interface: a molecular dynamics simulation”, Nanoscale, **12**, 17870-17879 (2020).

[29] C.U. Gonzalez-Valle, B. Ramos-Alvarado, “Molecular Dynamics Simulations of Wettability, Thermal Transport, and Interfacial Liquid Structuring and the Nanoscale in Polar Solid-Liquid Interfaces”, ACS Applied Nano Materials, **4**, 3821-3832 (2021).

[30] H. Asakawa et al., “Two types of quasi-liquid layers on ice crystals are formed kinetically”, PNAS, **113** (7), (2016), pp. 1749-1753.

[31] E. B. Moore and V. Molinero, “Is it cubic? Ice crystallization from deeply supercooled water”, Physical Chemistry Chemical Physics, **13**, (2011), pp. 20008-20016.

[32] T. Li, D. Donadio, G. Russo, G. Galli, “Homogeneous ice nucleation from supercooled water”, Physical Chemistry Chemical Physics, **13**, 19807–19813 (2011).

[33] Y. Ueki, S. Matsuo, M. Shibahara, “Molecular Dynamic Study of Local Interfacial Thermal Resistance of Solid-Liquid and Solid-Solid Interfaces: Water and Nanotextured Surface”, arXiv preprint, arXiv:2011.03184 (2020).

[34] Y. Ueki, S. Matsuo, M. Shibahara, “Molecular Dynamic Study of Local Interfacial Thermal Resistance of Solid-Liquid and Solid-Solid Interfaces: Water and Nanotextured Surface”, Proceedings of 8th International Symposium on Advances in Computational Heat Transfer, CHT-21-135, (2021).

[35] L. Hu et al., "Determination of interfacial thermal resistance at the nanoscale", Physical Review B, **83**, 195423 (2011).

[36] Z. Liang et al., "Thermal resistance at an interface between a crystal and its melt", The Journal of Chemical Physics, **141**, 014706 (2014).

[37] D. Surblys et al., "Molecular dynamics investigation of surface roughness scale effect on interfacial thermal conductance at solid-liquid interfaces", The Journal of Chemical Physics, **150**, 114705 (2019).

[38] C. U. Gonzalez-Valle, L. E. Paniagua-Guerra, and B. Ramos-Alvarado, “Implications of the Interface Modeling Approach on the Heat Transfer across Graphite–Water Interfaces”, The Journal of Physical Chemistry C, **123,** 36, 22311-22323 (2019).